EU contract number RII3-CT-2003-506395

CARE-Report-2006-036-PHIN
CARE-Note-2006-016-PHIN

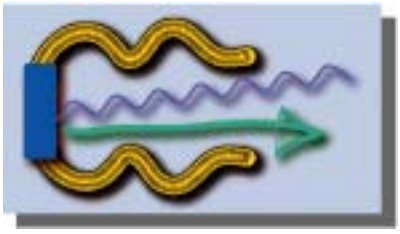

PHIN

Broadrange Single Shot Electron Spectrometer

Y. Glinec, J. Faure, A. Guemnie-Tafo, V. Malka
Laboratoire d'Optique Appliquée – ENSTA, UMR 7639,
CNRS, Ecole Polytechnique, 91761 Palaiseau, France

H. Monard, J.P. Larbre, V. De Waele, J.L. Marignier, M. Mostafavi
Laboratoire de Chimie Physique / ELYSE, Université Paris Sud 11, 91405 Orsay, France
(Dated: July 6, 2006)

Abstract

This article gives a detailed description of a single shot electron spectrometer which was used to characterize electron beams produced by laser-plasma interaction. Contrary to conventional electron sources, electron beams from laser-plasma accelerators can produce a broad range of energies. Therefore, diagnosing these electron spectra requires specific attention and experimental development. Here, we provide an analytical analysis of our compact magnetic system, followed by a detailed description of the scintillator and the CCD camera used to monitor the dispersed electron beam. An absolute calibration of the Lanex scintillator screen has been carried out on a laser-triggered radiofrequency picosecond electron accelerator. This absolute calibration is compared to charge measurements from an integrating current transformer for quasi-monoenergetic electron spectra from laser-plasma interaction.

Work supported by the European Community-Research Infrastructure Activity under the FP6 « Structuring the European Research Area » programme (CARE, contract number RII3-CT-2003-506395).

Broadrange single shot electron spectrometer

Y. Glinec, J. Faure, A. Guemnie-Tafo, V. Malka*
Laboratoire d'Optique Appliquée – ENSTA, UMR 7639, CNRS, École Polytechnique, 91761 Palaiseau, France

H. Monard, J.P. Larbre, V. De Waele, J.L. Marignier, M. Mostafavi
Laboratoire de Chimie Physique / ELYSE, Université Paris Sud 11, 91405 Orsay, France
(Dated: July 6, 2006)

This article gives a detailed description of a single shot electron spectrometer which was used to characterize electron beams produced by laser-plasma interaction. Contrary to conventional electron sources, electron beams from laser-plasma accelerators can produce a broad range of energies. Therefore, diagnosing these electron spectra requires specific attention and experimental development. Here, we provide an analytical analysis of our compact magnetic system, followed by a detailed description of the scintillator and the CCD camera used to monitor the dispersed electron beam. An absolute calibration of the Lanex scintillator screen has been carried out on a laser-triggered radiofrequency picosecond electron accelerator. This absolute calibration is compared to charge measurements from an integrating current transformer for quasi-monoenergetic electron spectra from laser-plasma interaction.

PACS numbers: 07.55.-w, 07.81.+a, 29.40.Mc, 52.38.Kd

I. INTRODUCTION

Laser-plasma accelerators have been intensively studied during the past years. In 1979, Tajima & Dawson [1] proposed to accelerate injected electrons in a plasma wave, which was driven by a laser pulse. When focusing an intense ultra-short laser pulse onto a helium gas jet, the medium is instantaneously fully ionized and the ponderomotive force of the laser expels the electrons from the laser axis. This creates a plasma wave behind the laser pulse, that propagates at the velocity of the laser pulse in the plasma (close to the celerity of light). This plasma wave corresponds to an electrostatic field that can be accelerating for electrons when properly injected. For sufficiently large laser intensities, electrons are self-injected in the plasma wave and gain relativistic energies in an electric field of about 1 TV/m. This exceeds by several orders of magnitude the maximum electric from conventional accelerators.

The electron spectrum can extend over a very broad range of energies. Thus, diagnosing properly such electron spectra requires an adapted electron spectrometer. Various kind of spectrometers have been reported for laser-plasma interaction. In earlier work, an imaging spectrometer composed of a tunable magnetic field and 4 silicon diodes was used [2]. Using a collimator, the central part of this electron beam was collected. The diodes and the imaging property of this spectrometer gave both a high energy resolution and a high sensitivity to electrons. The energy range of the diodes could be selected by varying the intensity of the current flowing inside the electro-magnet. However, in order to record a full spectrum, it was necessary to accumulate many shots while scanning the magnetic field of the spectrometer. In addition, a separate measurement of the electron beam divergence using radiochromic films was also necessary. This spectrometer was well-adapted for reproducible electron sources (typically with a Maxwellian-like spectrum).

Using imaging plates with a pair of magnets allowed the acquisition of the full electron spectrum in a single shot [3, 4]. This non-imaging magnetic system is compact and fits into an experimental chamber. But the processing of the screen is not adapted to a high-repetition rate laser system (10 Hz). Therefore, we have implemented a spectrometer which combines compact magnets, a phosphor screen (LANEX) and an Integrating Current Transformer (ICT) in order to record the whole spectrum of the electron beam in a single shot. Using this compact system, we have been able to measure a quasi-monoenergetic and high energy electron spectrum [5].

In this report, we summarize the characteristics and performances of this spectrometer. Sec. II describes the analytical and the experimental work related to the characterization of this detector. We point out that a specific difficulty of laser-plasma accelerators is to achieve a reliable measurement of the charge. Here, the charge is estimated through an absolute calibration of the Lanex film which was performed on ELYSE [13], a laser-triggered radiofrequency (RF) picosecond electron accelerator. The results are then extrapolated to our experimental conditions. Some examples of electron spectra using the absolute calibration are shown in Sec. III and a comparison is drawn with previous results using the ICT. This study was also used to design larger magnets for future GeV electron acceleration experiments.

*Electronic address: victor.malka@ensta.fr

EU contract number RII3-CT-2003-506395 CARE-Note-2006-016-PHIN

II. SPECTROMETER DESCRIPTION

A. Magnet system

We have used a simple magnet system consisting of two plane NdFeB magnets with length $L_m = 5$ cm, width $l_m = 2.5$ cm and height 1 cm, spaced by 1 cm of vacuum. The maximum magnetic field obtained is $B_m = 0.45$ T.

1. *Analytical dispersion equations*

First, the magnetic field is assumed to be uniform and equal to B_m between the two magnet parts, and a null field outside. The radius of curvature R of a relativistic electron with kinetic energy E_0 in a uniform magnetic field B_m can be simplified to $B_m R = E_0/(ec)$ for relativistic electrons, where e is the electron charge and c the celerity of light.

The geometric parameters which describe this system are : $Ds = 6$ cm the distance between the source and the magnet, $Dl = 17$ cm the distance between the magnet and the Lanex screen, $\theta_l = 55°$ the angle of the Lanex with respect to the transverse direction (see Fig.1).

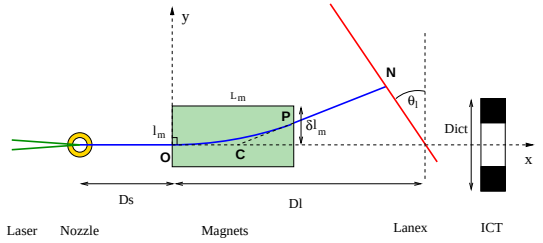

FIG. 1: Definition of all parameters used in the text. ICT stands for Integrating Current Transformer.

The electron trajectory can therefore be described by geometric shapes. It propagates on a straight line when no magnetic field is applied and it describes a circle arc inside the magnet. The origin is taken at the entrance of the electron in the magnet. We will assume here that incident electrons come along the (Ox) axis, perpendicular to the magnet's surface. Provided that the electron gets out at the opposite side of the magnet, the intersection of the circular trajectory and the end of the magnet in P has coordinates :

$$(x_P, y_P) = (L_m, R - \sqrt{R^2 - L_m^2}) \tag{1}$$

The holder of the magnet prevents electrons from going out through the lateral sides. Therefore, the minimum electron energy satisfies the relation $y_P = \delta l_m$, where $\delta l_m = 1.3$ cm is the maximum ordinate of the magnet.

Point C, which is the intersection of the tangent to the electron trajectory when it enters and exits the magnet, verifies $OC = CP$, leading to :

$$(x_C, y_C) = \big((x_P^2 + y_P^2)/(2x_P), 0\big) \tag{2}$$

And finally, the intersection in N of the electron trajectory with the scintillator screen along a straight forward line is given by :

$$(x_N, y_N) = \left(Dl - y_N \tan(\theta_l), \frac{(Dl - x_C)y_P}{x_P - x_C + y_P \tan(\theta_l)}\right) \tag{3}$$

In the following, we will write $s_N = y_N/cos(\theta_l)$ the path distance from the laser axis along the detector. Note that the same expressions are valid for a circular magnet with center in C and radius $R = OC$. In that case x_C becomes R.

2. *Effective magnetic field and dispersion*

The real magnetic field is not uniform and has a gradient length which is comparable to the distance between the magnets. The magnetic field was measured with a Hall probe and a Gauss meter along the longitudinal axis. The comparison with results from a code is shown in Fig. 2. The magnetic field becomes negative outside the magnet which decreases the overall dispersion efficiency. Since no attention was given to close the field lines outside the magnet, it is not surprising that the magnetic field inverses outside. The equivalent uniform magnetic field is shown in dashed line on this figure.

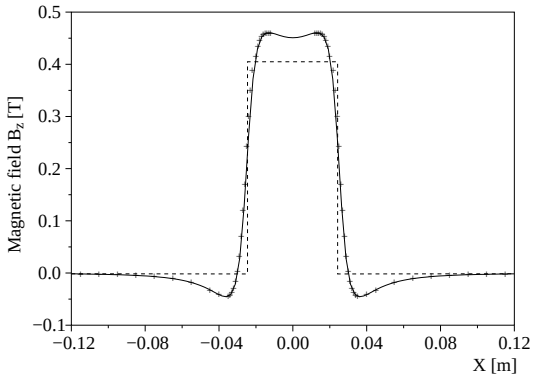

FIG. 2: Measured magnetic field B_z along the laser axis (plus), calculated magnetic field (line) and equivalent magnetic field for the analytical formulas (dash).

The effective magnetic field B_m^{eff} has been computed from these experimental data and is has the following expression :

$$B_m^{eff} = \frac{1}{L_m} \int_{-\infty}^{+\infty} B_z(x) dx \tag{4}$$

where $B_z(x)$ is the the projection of the magnetic field along the (Oz) axis, measured along the laser axis. In our experimental conditions, this value equals $B_m^{eff} = 0.41$ T.

The dispersion curve obtained with this effective magnetic field is shown on Fig. 3. It perfectly matches the

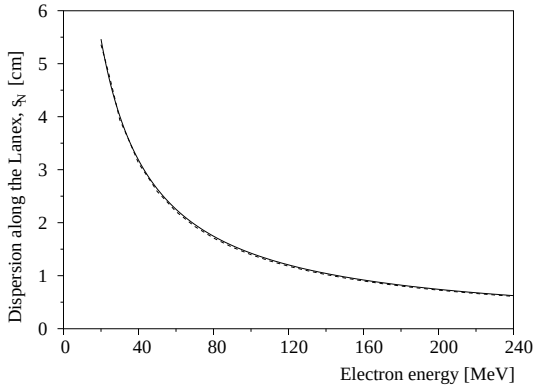

FIG. 3: Dispersion on the phosphor screen as function of the electron energy for analytical formulas (dashes) and for numerical simulations reproducing the real magnetic field (line).

dispersion computed by tracing electron trajectories in the computed map of magnetic field. The analytical formulas with the effective magnetic field will be used in the following. The uncertainty arising from the curve separation is negligible compared to the transverse size of the electron beam on the scintillator. The energy spread resulting from this natural divergence is the main limitation in resolution as described in the following.

3. Magnetic system resolution

The resolution of this spectrometer is mainly limited by the natural divergence of the electron beam. This was not taken into account in the analytical formulas, since we assumed that the incident electron was perpendicular to the magnets' surface. Even for a pure monoenergetic electron beam, the divergence angle would give an elliptic shape on the detector around the mean deviation angle. This divergence can be measured in the non-dispersive direction because no collimator is used here due to an already small electron beam divergence (about 10 mrad). In this study, we will neglect the edge focusing effect by the magnetic field at the boundary of the magnet [6]. To confirm this point, here is an estimation of the effects of these fields in the direction perpendicular to the dispersion plane. In the frame of thin magnetic lenses, the focal length for an electron beam with divergence $\theta_s \ll 1$ is $f \sim 2R/\theta_s$, where R is the gyroradius of the electron. If we assume a 100 MeV electron beam with divergence $\theta_s = 10$ mrad entering in a 1 T magnetic field, one obtains a focal length of 67 m, which is very long compared to the dimensions of the experiment.

This spread δz in the non-dispersive direction (Oz) leads to the spread along the detector in the dispersive plane $\delta_s = \delta z/\cos(\theta_\perp)$, where $\theta_\perp = \theta_l - \theta_e$ is the angle between the normal to the scintillator and the electron trajectory and $\theta_e = \arctan(y_P/(x_P - x_C))$ is the angle of the electron relative to the (Ox) axis (see Fig. 5). The corresponding energy range is $\delta E = \delta_s \div ds_N/dE$. If one assumes that $\delta_s \ll s_N \ll L_{tot}$, the resolution for an energy E_0 becomes

$$\frac{\delta E}{E_0} = \frac{\delta_s}{E_0} \div \frac{ds_N}{dE} \underset{E_0 \to \infty}{\sim} \frac{(Ds + Dl)R\theta_s}{(Dl - L_m/2)L_m} \qquad (5)$$

This resolution degrades linearly with the electron energy E_0, contained in radius R. For instance, using the typical experimental parameters given in the text, we have a resolution of 6, 14, 27, 53% respectively for 20, 50, 100, 200 MeV electrons. This work has been used to manufacture two larger magnets giving better resolution at high energy. One is 10 cm long and provides 1 T between the two magnets to increase the resolution around 200 MeV. The other one is 40 cm long for acceleration to the GeV level.

B. Detection system

1. Corrections applied on the raw signal

The light emitted by the Lanex screen comes from the phosphor layer. We assume in this study that the energy emitted in the visible range by this screen is proportional to the amount of energy deposited in the scintillator layer. This means that we will neglect the non-radiative energy loss (quenching effect). As shown for an imaging plate (Film Fuji BAS-SR2025) [3], the energy deposited in the detector becomes almost independent of the incident electron energy above 1 MeV and it was verified experimentally for 11.5, 30 and 100 MeV electrons. We remind that the direct use of collisional stopping power [7] is inappropriate to obtain the energy deposited in the scintillator layer, because many of the secondary particles will exit the scintillator and deposit their energy further away. Therefore, we have also performed a Monte-Carlo simulation using `Geant4` [8] of the energy deposited in Lanex Kodak fine screen, the layer composition of which is given in Table I. A protective 100 μm-thick aluminium screen, which is used in the experiments to shield the detector from the laser light, is simulated in front of the scintillator. The electrons are sent perpendicular to the Lanex surface. The free parameter `CutRange` which is the threshold for the production of secondary particles is set to 5 μm.

Figure 4 shows the energy deposited in the scintillator layer which emits light. The curve becomes almost flat at high energy. The signal peaks at 450 keV at lower energy. This is the consequence of the decrease of the electron kinetic energy as it propagates in the medium. Its collisional cross section increases fast until it stops. For very low energy, the electrons don't cross the first layers of the detector (mainly the aluminium foil and the substrate) and no energy is deposited in the sensitive layer.

The corrections that should be applied on the raw signal to retrieve the spectrum are : (i) a correction due

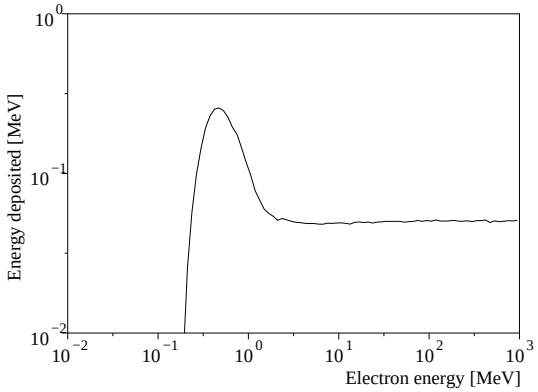

FIG. 4: Energy deposited in the scintillator layer of Lanex Kodak Fine screen for different electron energies.

to the variation of the stopping power (which was shown to be negligible), (ii) a differential element ds_N/dE corresponding to the decrease of dispersion as the electron energy increases (see Sec. II A 1). The amplitude of the spectrum, plotted on a linear scale, can be determined in two different ways. In the first case, we evaluated the yield of the whole detection system to obtain the number of electrons. In the second case, we measured the number of electrons with an ICT.

C. Absolute calibration

1. *Intrinsic efficiency*

The absolute measurement of the spectrum with the Kodak Lanex Fine screen requires a full description of this material [9] and the layer description is reproduced in Table I. In particular, the scintillator is composed of a mixture of phosphor powder (Gd_2O_2S:Tb, $\rho_{GOS} = 7.44$ g/cm^3) in a urethane binder (see Fig. 5). The phosphor surface loading is $h_S = 33$ mg/cm^2. We will focus the next part of this calibration on the powder contained in the scintillator since only this material emits light.

Item	Material	Density (g/cm^3)	Thickness (cm)
Laser shielding			
aluminium shielding	aluminium	2.7	0.0100
Kodak Lanex Fine screen			
protective coating	cellulose acetate	1.32	0.0010
plastic substrate	poly(ethylene terephtalate)	1.38	0.0178
scintillator	Gd_2O_2S + urethane binder	4.25	0.0084
protective coating	cellulose acetate	1.32	0.0005

TABLE I: Composition of the Lanex screen.

The description of the phosphor screen and the imaging system was already presented for an incident X-ray beam [10] and a proton beam [11]. However, as explained by S. N. Boon, there exist no data for Lanex efficiency for protons or energetic electrons. The intrinsic energy conversion efficiency ε in Gd_2O_2S:Tb, which is the ratio of energy deposited in Gd_2O_2S which is converted into visible light, was calculated for X-rays in [12]. It was found to vary between 15 % and 20 %. For several reasons, this might not be accurate for our electron beam : (i) manufacturers of phosphor screens have no idea of the linearity of their detector for such high electron fluency, (ii) this intrinsic conversion efficiency depends also of the nature and the energy of the incoming particle. Previous studies were performed for X-rays with energies between 20 and 70 keV. In the frame of this study, the intrinsic conversion efficiency is the only unknown parameter required for an absolute calibration of the electron spectrum.

Consequently, the calibration of this scintillator has been performed at ELYSE, a RF accelerator in Orsay designed for radiolysis experiments [13]. Its photocathode produces electron bunches containing a maximum of 5 nC, which are accelerated at a maximum energy of 9 MeV. For our experiment, the accelerator delivered 15 ps-long pulses, at 1 Hz repetition rate to ensure a thermal stability of the scintillator. The bunch charge was also decreased to 3 nC to be as close as possible to our typical experimental conditions. At the output of the accelerator, the electron beam exits the vacuum system through a 12 μm-thick aluminium foil (see Fig. 6). The electrons then propagate in the air through the core of the ICT and then inside the scintillator, placed perpendicular to the beam axis. The signal is imaged at 45° onto a Charge Coupled Device (CCD) camera placed at 61 cm from the scintillator. The exposure time is set to 90 ms, equal to the exposure time during experiments, which is much longer than the relaxation time of the scintillator (of the order of a few milliseconds). We have also used an interference filter at 546 nm to reproduce our usual experimental conditions. The scattering of the electrons in the aluminium foil requires that the ICT and the scintillator be as close as possible to the aluminium foil. Because all electrons go through the core of the ICT and because there is no electromagnetic noise, the ICT gave a charge for each shot consistent with an independent measurement done with a Faraday cup, placed in the beam path. We have worked at three different energies : 3.3, 4.8 and 8.5 MeV and we checked that the dark current level was very low.

The integrated number of counts after substraction of

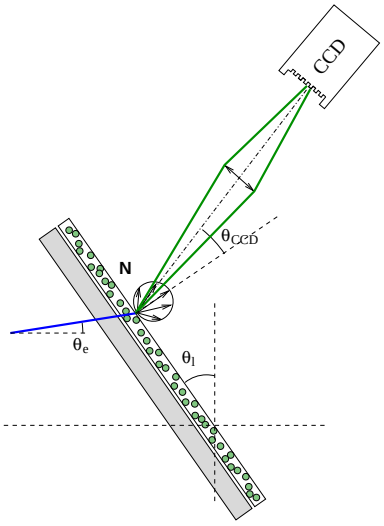

FIG. 5: Lanex screen, optical imaging device and associated parameters.

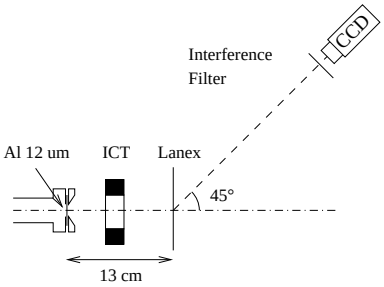

FIG. 6: Setup for the calibration of the LANEX scintillator

the background and the dark current is linear with the incident charge (see Fig. 7). Figure 8 shows the evolution of the ratio between this integrated number of counts and the charge measured by the ICT for 3 different electron energies. This ratio is independent of the electron energy, as expected from the Monte-Carlo simulations (in Fig. 4). The errorbars are bigger at 8.5 MeV because the signal also contains X-rays that perturb the analysis. From the experimental geometry and using the analytical equations, one obtains the yield of kinetic energy of an electron which is transformed into visible light into the scintillator expressed in unit of pure gadolinium oxysulfide (GOS) thickness $\varepsilon dE/dx = 1.8 \pm 0.2$ MeV/cm. Using the dose deposition estimated from the previous Monte-Carlo simulation, this surprisingly leads to $\varepsilon = 16\% \pm 2\%$, which is close to the value reported for X-rays [12].

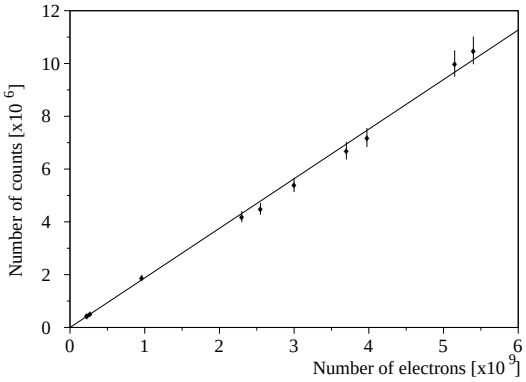

FIG. 7: Evolution of the signal intensity with the charge for 3.3 MeV electron energy

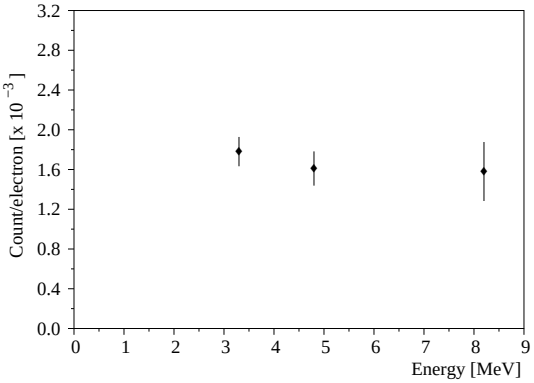

FIG. 8: Ratio between the integrated number of counts on the CCD and number of electrons measured by the ICT for an electron energy of 3.0, 4.8 and 8.5 MeV. The errorbars account for the statistical fluctuations for each energy and the uncertainty from the analysis itself (due to X-rays substraction).

2. *Yield of the detector*

The number of photons N_{cr} created in the scintillator at the central wavelength per incident electron is :

$$\frac{dN_{cr}}{dN_{el}} = \frac{1}{E_{ph}} \, \varepsilon \, \frac{dE}{dx} \, \delta x \tag{6}$$

where $\delta x = h_S/(\rho_{GOS} \cos(\theta_\perp))$ is the equivalent thickness of pure GOS crossed by an electron and $E_{ph} = 2.27$ eV the energy of one photon emitted at 546 nm. The other lines in the emission spectrum will be damped by the interference filter placed before the CCD camera.

Photons created will experience multiple scattering in the medium and at the boundary, due to optical index variation. The output fraction of light which escapes the screen is estimated in [10]. By extrapolating the curve to our phosphor load density, the transmission output factor is $\zeta = 22\%$. The angular distribution of photons which escape the screen is close to a Lambertian law (co-

sine) [14]. According to G. E. Giakoumakis *et al*, this law is well suited for hard X-ray radiation, where the energy deposition along the propagation axis is more homogeneous. In our case, the high kinetic energy of the electrons leads to a dose deposition almost independant of the depth. They also point out that the angle of incidence of the electrons relative to the screen surface had no important influence. Therefore, the number of photons collected by the detector on a single pixel per photon created is

$$\frac{dN_{coll}}{dN_{cr}} = \zeta \; g(\theta_{CCD}) \; \delta\Omega \; q_l \; q_Q \; q_{IF} \tag{7}$$

where $g(\theta_{CCD}) = \cos(\theta_{CCD})/\pi$ is the normalized Lambertian law at the angle of the CCD camera, $\delta\Omega = 2.0 \times 10^{-3}$ sr is the solid angle of collection. $q_l = q_Q = 0.95$ and $q_{IF} = 0.20$ are respectively the transmission factors of the lens, the quartz window in front of the CCD and the interference filter. The interference filter coefficient is the fraction of energy in the emission spectrum of the scintillator in the visible which is transmitted through the interference filter.

We used a 16 bit CCD Andor camera, model DV420-FI for our detection. The quantum efficiency (number of electrons produced for one optical photon) of the camera at -20° C and 546 nm is about $QE = 26\%$ and $r = 7$ electrons are needed to create one count (for a readout time of 16 μs per pixel). The CCD yield is

$$\frac{dN_{cts}}{dN_{coll}} = \frac{QE}{r} \tag{8}$$

From the signal measured on the CCD camera, we have the number of counts for each pixel. The incoming electron spectrum is obtained from the following relation :

$$\frac{dN_{el}}{dE}(E_0) = \frac{Cts(E_0)}{\delta s_{pix}} \frac{ds_N}{dE} \div \left(\frac{dN_{cts}}{dN_{coll}} \; \frac{dN_{coll}}{dN_{cr}} \; \frac{dN_{cr}}{dN_{el}} \right) \tag{9}$$

where $Cts(E_0)$ is the number of counts from the pixels of the CCD corresponding to an energy E_0 (integrated along the non-dispersing plane) and δs_{pix} mm is the size of a pixel (27 μm) projected along the Lanex screen.

D. Calibration from the ICT

During laser-plasma interaction experiments, we have used a combination of an Integrating Current Transformer (Bergoz ICT-055-070-20:1) and a Beam Charge Monitor (Bergoz BCM-RRS/B) to measure the charge in a given part of the spectrum. This ICT is placed behind the Lanex screen, on the laser axis and records the high energy part of the electron spectrum. First, the value given by this device may not be accurate in our experiments for several reasons : (i) it was not designed to measure electron bunches as short as a 100 fs. However, the Beam Charge Monitor integrates the oscillations and should give an accurate signal as explained by the manufacturer. (ii) The influence of electrons that travel inside the spires or just in the vicinity of the ICT is not well known. A perfect ICT should give a null flux for electrons flowing outside. Electrons should be flowing inside the core of the ICT. (iii) The electronic system is also expected to be sensitive to the electromagnetic field produced during the interaction. Due to size limitations, we have placed this ICT as far as possible from the interaction point ($\sim$ 50 cm). We have also protected the ICT from direct laser light using a protective layer in Teflon. (iv) Finally, this device is also sensitive to the huge amount of low energy electrons which are emitted in all directions from the interaction point. They may contribute significantly to the measured charge. In order to block these low-energy electrons, we have added lead shielding all around the magnet.

The number of counts on the CCD was corrected for the energy dispersion and energy deposition. In the frame of this study, the number of electrons dN_{el}/dE with energy between E_0 and $E_0 + dE$ is proportional to $f(E_0)$

$$f(E_0) = Cts(E_0) \frac{ds_N}{dE} \tag{10}$$

where $Cts(E_0)$ is the number of counts from the pixels of the CCD corresponding to an energy E_0 (integrated along the non-dispersing direction), ds_N/dE is the energy dispersion. Then, the final spectrum dN_{el}/dE is derived from $f(E_0)$ by normalizing the signal above E_{ICT} (defined as the minimum energy intercepted by the ICT) to the number of electrons measured by the ICT.

However, the effective diameter of the ICT was difficult to determine. We have calculated the amplitude of the spectrum for two extreme cases : the inner (55 mm) and outer diameter (100 mm). This ICT was placed on the laser axis. Due to the magnetic field, only the most energetic electrons were collected by this device (above $E_{ICT} = 110$ and 50 MeV in our configuration respectively for the inner and outer diameter). We obtained the charge at high energy, which was used to evaluate the electron spectrum amplitude. The charge contained in the peak of the spectrum changed by 50% with these two diameters. This explains the large error bars in the measured charge in the quasi-monoenergetic peak published in Ref. [5] ($Q = 0.5 \pm 0.25$ nC).

III. EXPERIMENTAL RESULTS

A. Quasimonoenergetic electron beams

Figure 9 shows some examples of quasi-monoenergetic electron spectra obtained in laser-plasma interaction. The corresponding raw image is shown in the inset. The horizontal axis on these images gives the electron energy on a non-linear scale, whereas the vertical axis gives the electron beam divergence, which limits the resolution.

Under optimal interaction conditions, the divergence of the beam is usually below 10 mrad at full width at half maximum (FWHM). These spectra were obtained under different experimental conditions (interaction parameters and spectrometer configuration may vary). The absolute calibration is used here to obtain the amplitude of the spectrum (eq 9).

Curve a) shows a quasi-monoenergetic spectrum peaked at high energy. The charge in the peak ($120 < E < 160$ MeV) is 9 pC. Even if the raw image reveals a sharp and bright spot at high energy, this peak might be broadened and smoothed during the deconvolution process. This is mainly because this spectrometer lacks resolution for high energy. However, for this shot the relative energy spread is 6% FWHM. One can also note the low number of electrons at low energy for this image. Curve b) shows a spectrum around 85 MeV, for which the resolution is adapted. For this shot, the charge reaches 250 pC ($E > 55$ MeV). Even if the signal at low energy is very weak, the spectrum after deconvolution shows a significant emphasize of the low energy electrons.

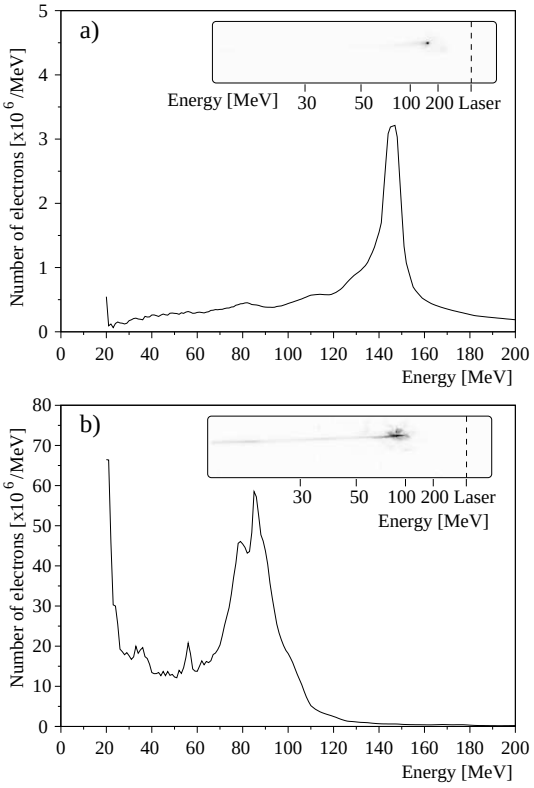

FIG. 9: Examples of spectra obtained after deconvolution of the images shown in inset. The amplitude is determined using the absolute calibration of the detector. The y-axis scales are not the same.

Using a more dispersive magnet or an imaging spectrometer should enhance the contrast between the quasi-monoenergetic peak and low-energy electrons. Since the dispersion on the screen is non linear, this kind of spectrometer is well adapted to a given range of electron energy. The lowest energy is limited by the size of the Lanex screen and the highest by the natural divergence of the electron beam.

B. Discussion

We discuss here the differences between the two calibration methods, which only affect the spectrum amplitude. Unfortunately, when applying both methods on a same image, different amplitudes are obtained. The ratio varies depending on the analyzed image, revealing a lack of correlation. For instance, we have obtained an amplitude 8 times smaller when using the absolute calibration. Even if a lot of care has been devoted to the shielding of the ICT, it seems that this device remains sensitive to the electrical noise. This is a major issue because many groups are using an Integrating Current Transformer to estimate the bunch charge [5, 15–17]. This system might not be reliable in our experimental conditions.

It seems that the absolute calibration gives the most accurate estimation of the charge. We still obtain electron peaks containing several hundreds of pC in the peak, which is consistent with the physical scenario. However, some assumptions have also been performed for this calibration: we have extrapolated the calibration from a RF accelerator to our experimental conditions. But the scintillation efficiency might be different for very dense, ultra-short (sub 100 fs) electron bunches. However, there exist no data yet under such irradiation conditions. One has to assume that the corrections won't significantly affect the yield. We have never seen any saturation effect with this scintillator.

Other techniques have been developed to retrieve the amplitude, using diodes [2, 18] or the calibration of an imaging plate [19, 20]. They all require the same assumptions, that the yield of electron-hole pairs or the scintillation efficiency remains constant.

IV. CONCLUSION

This paper summarizes the work performed to design and build a broadrange single shot electron spectrometer. The analytical formulas giving the impact distance and the resolution along the Lanex screen are explained. The effective magnetic field is measured and used to compute the dispersion. Using a home-made spectrometer, we were able to record new features of the electron beam : a quasi-monoenergetic peak at high energy. The amplitude of the spectra is determined in two separate ways : using the absolute calibration of the scintillator performed on a radiofrequency accelerator or an Integrating Current Transformer. The two calibration methods differ significantly. The ICT is thought to be sensitive to electromagnetic perturbation during the interaction. The absolute calibration is expected to be more reliable

but it requires the assumption that the calibration can be extrapolated to our experimental conditions. This assumption is also implicitly used by all other calibrations performed. This report points out the difficulty of evaluating the charge in our experiments.

V. ACKNOWLEDGMENTS

The authors would like to acknowledge the fruitful discussions with Dr M. Kando from the Japan Atomic Energy Research Institute, with Dr D. Neely from Rutherford Appleton Laboratory and with Pr. Y.A. Gauduel from Laboratoire d'Optique Appliquée. This work was supported by the European Community Research Infrastructure Activity under the FP6 "Structuring the European Research Area" program (CARE, contract number RII3-CT-2003-506395).

[1] T. Tajima and J. Dawson, Phys. Rev. Lett. **43**, 267 (1979).
[2] V. Malka *et al*, Physics of Plasmas **8**, 2605 (2001).
[3] K. Tanaka *et al.*, Rev. Sci. Instr. **76**, 013507 (2005).
[4] C. Clayton, K. Marsh, C. Joshi, C. Darrow, A. dangor, A. Modena, Z. Najmudin, and V. Malka, in *Proceedings of the 1995 Particle Accelerator Conference and International Conference on High-Energy Accelerators* (1995), ISBN 0-7803-2937-6.
[5] J. Faure *et al.*, Nature **431**, 541 (2004).
[6] S. Humphries, *Principles of charged particle acceleration* (Wiley-Interscience, New-York, 1986), sec. 6.8, 6.9 et 6.10.
[7] Tech. Rep. 37, International Commission on Radiation Units and Measurements (ICRU) (1984).
[8] Agostinelli S. *et al*, Nucl. Instr. Meth. A **506**, 250 (2003).
[9] A. E. Schach von Wittenau, C. M. Logan, M. B. Aufderheide, and D. M. Slone, Med. Phys. **29**, 2559 (2002).
[10] T. Radcliffe, G. Barnea, B. Wowk, R. Rajapakshe, and S. Shalev, Med. Phys. **20**, 1161 (1993).
[11] S. N. Boon, *Dosimetry and quality control of scanning proton beams* (University Library Groningen, 1998).
[12] G. E. Giakoumakis, C. D. Nomicos, and P. X. Sandilos, Phys. Med. Biol. **34**, 673 (1989).
[13] J. Belloni, H. Monard, F. Gobert, J. Larbre, A. Demarque, V. De Waele, I. Lampre, J. Marignier, M. Mostafavi, J. Bourdon, et al., Nucl. Instr. & Meth. in Phys. Research A **539**, 527 (2005).
[14] G. E. Giakoumakis and D. M. Miliotis, Phys. Med. Biol. **30**, 21 (1985).
[15] C. G. R. Geddes *et al.*, Nature **431**, 538 (2004).
[16] T. Hosokai, K. Kinoshita, T. Ohkubo, A. Maekawa, and M. Uesaka, Phys. Rev. E **73**, 036407 (2006).
[17] C. Hsieh, C. Huang, C. Chang, Y. Ho, Y. Chen, J. Lin, J. Wang, and S. Chen, Phys. Rev. Lett. **96**, 095001 (2006).
[18] S. Mangles, C. D. Murphy, Z. Najmudin, A. G. R. Thomas, J. L. Collier, A. E. Dangor, A. J. Divall, P. S. Foster, J. G. Gallacher, C. J. Hooker, et al., Nature **431**, 535 (2004).
[19] E. Miura, K. Koyama, S. Kato, S. Saito, M. Adachi, Y. Kawada, T. Nakamura, and M. Tanimoto, Appl. Phys. Lett. **86**, 251501 (2005).
[20] B. Hidding *et al.*, Phys. Rev. Lett. **96**, 105004 (2006).